

Nanoscale subsurface dynamics of solids upon high-intensity laser irradiation observed by femtosecond grazing-incidence x-ray scattering

Lisa Randolph,¹ Mohammadreza Banjafar,^{2,3} Thomas R. Preston,² Toshinori Yabuuchi,^{4,5} Mikako Makita,² Nicholas P. Dover,⁶ Christian Rödel,⁷ Sebastian Göde,² Yuichi Inubushi,^{4,5}

Gerhard Jakob,⁸ Johannes Kaa,² Akira Kon,⁶ James K. Koga,⁶ Dmitriy Ksenzov,¹ Takeshi Matsuoka,^{9,10} Mamiko Nishiuchi,⁶ Michael Paulus,¹¹ Frederic Schon,¹ Keiichi Sueda,⁵ Yasuhiko Sentoku,^{10,12} Tadashi Togashi,^{4,5} Mehran Vafae-Khanjani,⁸ Michael Bussmann,¹³ Thomas E. Cowan,^{3,13} Mathias Kläui,⁸ Carsten Fortmann-Grote,² Adrian P. Mancuso,^{2,14} Thomas Kluge,¹³ Christian Gutt,^{1,*} and Motoaki Nakatsutsumi^{2,9,†}

¹*Department Physik, Universität Siegen, Walter-Flex-Str. 3, 57072, Siegen, Germany*

²*European XFEL, Holzkoppel 4, 22869, Schenefeld, Germany*

³*Technical University Dresden, 01069 Dresden, Germany*

⁴*Japan Synchrotron Radiation Research Institute (JASRI), Sayo, Hyogo, 679-5198, Japan*

⁵*RIKEN SPring-8 Center, Sayo, Hyogo 679-5148, Japan*

⁶*QST-Kansai, KPSI,8-1-7 Umemi-dai, Kizugawa-city, Kyoto, 619-0215, Japan*

⁷*Technical University Darmstadt, Schlossgartenstraße 9, 64289 Darmstadt, Germany*

⁸*Universität Mainz, Staudinger Weg 7, 55128 Mainz, Germany*

⁹*Open and Transdisciplinary Research Institute,*

Osaka University, Suita, Osaka 565-0087, Japan

¹⁰*Graduate School of Engineering, Osaka University, Suita, Osaka 565-0087, Japan*

¹¹*Technical University Dortmund, Otto-Hahn Straße 4, 44227 Dortmund, Germany*

¹²*Institute of Laser Engineering, Osaka University, Suita, Osaka 565-0871, Japan*

¹³*Helmholtz-Zentrum Dresden-Rossendorf, Bautzner Landstraße 400, 01328, Dresden, Germany*

¹⁴*Department of Chemistry and Physics, La Trobe Institute for Molecular Science,*

La Trobe University, Melbourne, Victoria 3086, Australia

(Dated: May 29, 2022)

Observing ultrafast structural changes in nanoscale systems is essential for understanding the dynamics of intense light-matter interactions, which play a pivotal role in material processing [1, 2], ultrafast phase transitions [3] and diagnosis of matter under extreme conditions [4]. One of the most relevant applications of femtosecond laser plasma interactions is laser machining and surface structuring [5]. For laser intensities on the order of 10^{14} W/cm², collisional plasmas are generated at the surface and subsequent transport processes such as electron-ion thermalization, melting and resolidification occur at picosecond and nanosecond time scales [6, 7]. Experimental techniques with nanometer spatial and femtosecond temporal resolution are required to test physical models and obtain quantitative measurements of the subsurface plasma dynamics. Here, we demonstrate grazing-incidence small-angle x-ray scattering (GISAXS) using x-ray free electron laser (XFEL) pulses allowing the *in situ* visualization of subsurface plasma dynamics with nanometer depth resolution. We measure the surface ablation and plasma density perturbation of multilayer samples following the femtosecond laser pulse interaction. This new methodology opens new possibilities for accurate characterization of subsurface dynamics in various applications of high-intensity laser-solid interactions including laser ablation, creation of warm dense matter, dynamic compression, and relativistic laser plasmas.

MAIN

With the advent of the chirped pulse amplification technique [8], intensities ranging from 10^{13} W/cm² to 10^{22} W/cm² can be achieved by focusing femtosecond laser systems to small spot sizes. The intensity regime around 10^{14} W/cm² is particu-

larly interesting for studies of atomic and molecular physics [9] but also for laser material processing [5]. When a laser pulse is focused on a solid surface at these intensities, the atoms at the surface are ionized and a dense plasma is created. During the femtosecond laser interaction, the laser field interacts with the electrons within a depth of a few tens of nanometers – the so-called skin depth – due

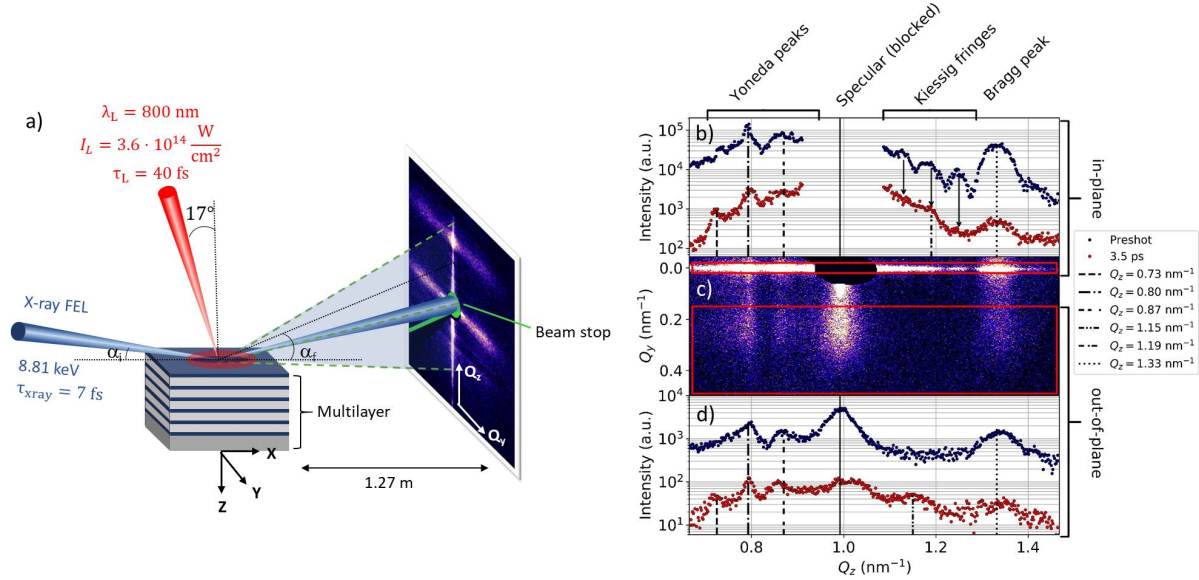


FIG. 1. Schematics of the experimental setup for the grazing incidence small-angle x-ray scattering (GISAXS) to investigate the subsurface dynamics of a solid-density plasma and typical GISAXS data obtained in a single shot. **a)** The multilayer (ML) sample consisted of 5 repeated layers of tantalum (Ta) and copper nitride (Cu_3N), of 4.3 / 11.5 nm thickness each, is irradiated by an optical laser (800 nm wavelength, $3.6 \pm 0.2 \times 10^{14} \text{ W/cm}^2$ intensity, 40 fs duration in full-width at half-maximum (FWHM)) with 17° incident angle from the sample normal with p-polarization. The x-rays (8.81 keV photon energy, 7 fs duration, 4 μm FWHM) irradiate the sample at a grazing incidence angle of 0.64° (thus elongated to 360 μm along the x-ray axis), i.e., slightly above the critical angle of external total reflection of the layer materials. The laser beam is defocused to obtain 500 μm diameter to cover the x-ray footprint. Scattered x-ray photons are recorded by an MPCCD area detector placed around the specular direction. The strong specular peak at $Q_z = 0.99 \text{ nm}^{-1}$ is blocked. **c)** Raw scattering signal from the cold sample without laser excitation (preshot). **b)** Lineout of the in-plane scattering as indicated by the red square on the upper side in **c)** for the preshot (upper line, blue) and 3.5 ps after laser irradiation (lower, red). The lineouts are artificially shifted vertically to aid comparison. **d)** Lineout for the out-of-plane scattering indicated by the lower red square in **c)**.

to the shielding of the laser field by high-frequency plasma oscillations. Several physical processes occur after the laser pulse on a femtosecond to nanosecond time scale leading to thermalization, diffusion, ablation that finally forms a new surface structure after resolidification [2]. A good control of these processes enables high-precision material processing [5, 10] and functional surfaces production [11]. At laser intensities of $10^{16} - 10^{22} \text{ W/cm}^2$, high-density plasmas can be used as active optical devices to manipulate the temporal [12] and spatial [13, 14] properties of laser radiation, as well as to generate coherent attosecond pulses in the extreme ultraviolet [15]. Furthermore, high intensity laser interactions with solids has attracted great

interest in the prospect of creating compact laser-driven particle [16] and gamma-ray sources [17]. In these experiments, the surface density profile is often perturbed before the arrival of the laser pulse due to imperfect temporal contrast, or during the pulse due to the extreme light pressure [18]. These interactions modify the transient optical properties of surface plasmas and influence the laser-plasma coupling mechanisms [19]. *In situ* visualization of the surface and subsurface density profile with skin-depth resolution is therefore crucial for numerous applications. Measurements of the dissipation dynamics of such non-uniform, non-equilibrium plasmas would enable the benchmarking of models of transport properties under

high-energy-density conditions and validate simulations, which are also relevant for laboratory experiments on astrophysics [20] and thermonuclear fusion [21].

So far, surface plasma dynamics have been widely investigated using femtosecond optical laser pulses [22, 23], where various surface-sensitive optical interferometry [23, 24] and spectroscopy [25] methods have been applied. For resolving physical processes under the surface and in the bulk, x-ray pulses appeared being more suitable. Experiments using ultrafast x-ray diffraction revealed, for example, non-thermal melting [26], coherent lattice vibrations [27], and ultrafast phase transitions [28]. Ultrafast deformation within a thin metal film has been studied using laser-driven soft x-ray sources [29]. Recently, femtosecond x-ray pulses from XFELs have been applied to investigate laser produced plasmas. Small angle scattering of femtosecond x-rays has revealed density gradients of expanding solid-density plasmas with nanometer resolution [30, 31]. However, these methods generally lack depth information from the interaction surface region into the bulk. In contrast, absorption and phase contrast x-ray imaging [32, 33] can indeed visualize bulk density profiles, but the resolution is limited to about 100 nm and is thus larger than the skin depth.

In this Letter, we report the demonstration of ultrafast grazing-incidence small-angle x-ray scattering (GISAXS) for visualizing the transient surface and subsurface density profiles with nanometer depth resolution. A measurement of the non-specular diffuse scattering pattern provides access to different depths of the sample under investigation. This will open the door to quantitative assessment of ultrafast, nanoscale density dynamics of high-density materials.

The experiment was performed at the EH6 station at the SACLA XFEL facility in Japan [34]. A metallic multilayer (ML) sample was irradiated by an optical laser with a central wavelength of 800 nm, intensity $3.6 \pm 0.2 \times 10^{14}$ W/cm² and pulse duration of 40 fs (Fig. 1 a). After a variable delay, the sample was irradiated with x-rays at a photon energy of 8.81 keV and a grazing incidence angle of 0.64°. Scattered x-ray photons were recorded by an MPCCD area detector [35] where the strong specular peak (incident angle equals the exit an-

gle, $Q_{\text{specular}} = 0.99 \text{ nm}^{-1}$) was blocked by a beam stop. Due to the shallow angle-of-incidence, the detected x-ray signal was integrated over ~ 1.2 ps (see *Methods* for more detailed description of the setup). Fig. 1 b-d) shows a typical x-ray diffuse scattering pattern obtained in a single shot as well as its lineouts along the Q_z direction (red and blue points in b) and d)). Both in-plane ($Q_y = 0$, Fig. 1 b) and out-of-plane ($Q_y \neq 0$, Fig. 1 d) scattering patterns contain information on the density profile along the z -direction (depth) [36]. The pattern at $Q_z > Q_{\text{specular}}$ is closely associated with the specular reflectivity curve [36] which we characterised separately *ex situ* (see *Methods*). Strong changes are observed between before (preshot, blue points) and after (3.5 ps, red points) the laser irradiation. The Bragg peak at $Q_z = 1.33 \text{ nm}^{-1}$ represents the typical length scale of each double layer (15.8 nm thick), and the small peaks between $Q_z = 0.99 \text{ nm}^{-1}$ and 1.33 nm^{-1} (Kiessig fringes [37]) are a fingerprint of the number of double layer repeats in the ML sample. Those peaks are weakened and suppressed after the laser irradiation. On the other hand, the peaks located at smaller $Q_z < Q_{\text{specular}}$ appear when the exit angle is equal to the critical angle of total external reflection, where the evanescent x-ray wave travels parallel to the surface (Yoneda peaks [38]). The peaks at 0.80 nm^{-1} and 0.87 nm^{-1} correspond to solid density of Cu₃N and Ta, respectively. These peaks are therefore sensitive markers for the uppermost surface layers. After the laser irradiation, a new Yoneda peak appeared around $Q_z = 0.73 \text{ nm}^{-1}$. It is worth mentioning that the analysis of the diffuse scattering signal and the Yoneda peaks is also referred to as grazing-incidence x-ray diffuse scattering [39]. We call the method GISAXS here as this is the most common term for this method at synchrotrons [40]. GISAXS has the advantage that depth information is provided without scanning the angles in contrast to x-ray reflectometry [36, 41].

In order to perform quantitative analysis, we use the program BornAgain [43] to retrieve the depth-resolved real-space density profile from the scattering data. Here, both in-plane and out-of-plane data are refined simultaneously which was crucial to obtain unique solutions (details in *Supplementary Information*). Figs. 2 a-b) show the in-plane

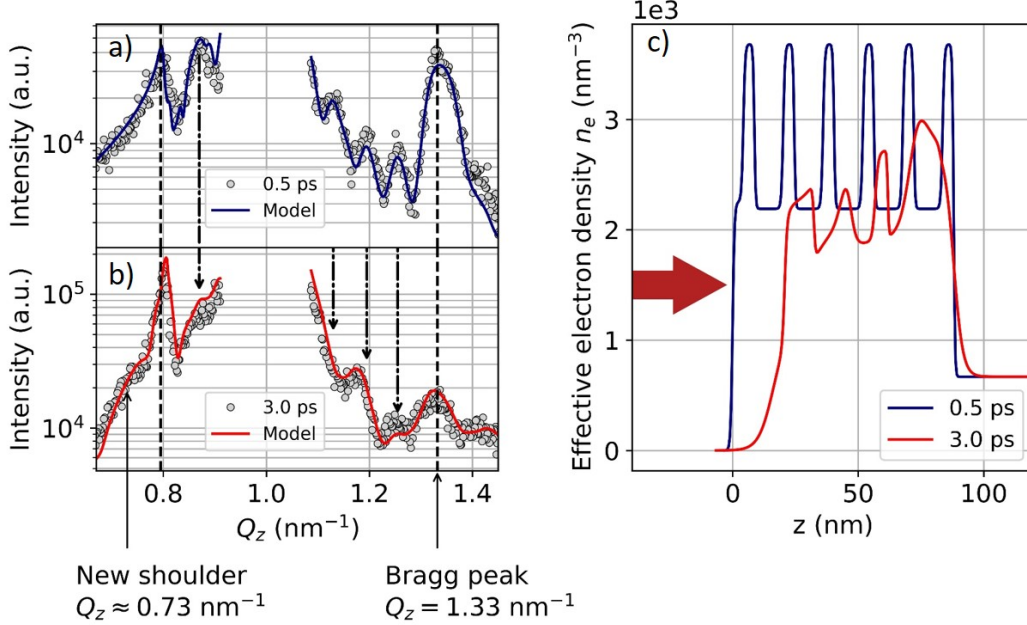


FIG. 2. **Obtained GISAXS signals and corresponding retrieved real-space effective electron density profiles.** Lineout of the in-plane scattering at **a)** 0.5 ps and **b)** 3 ps after the laser irradiation. **c)** Retrieved real-space effective electron density profile from the scattering data using the program BornAgain. The x-ray and laser parameters are the same as 1. The red arrow indicates the laser irradiation direction. The x-ray probe (8.81 keV) is sensitive to the electrons with binding energies below the photon energy, i.e., 27 and 63 electrons (= effective electrons) per Cu(29) and Ta(73) atoms – total electrons in parentheses. Due to the relatively small mean ionization ($Z_{mean} = 4 - 6$ [42]) what is essentially measured here are the bound electrons.

scattering profile obtained at 0.5 ps and 3.0 ps after laser irradiation, respectively, while Fig. 2 c) shows the corresponding retrieved electron density profile. Note that our x-ray probe is sensitive to the electrons with binding energies below the photon energy, i.e., 27 and 63 electrons (= effective electrons) for each Cu and Ta atom, respectively. Due to the relatively small mean ionization predicted under our laser condition ($Z_{mean} = 4 - 6$ [42]), what is essentially measured are the bound electrons, or equivalently, ion motion. The solid lines on the scattering pattern in Fig. 2 a-b) represent the density profiles obtained by the model through iteratively minimizing the chi-square values (*Supplementary Information*). The 0.5 ps signal is identical to the density profile in the cold sample. At 3.0 ps delay, the density profile is strongly modulated, although there still exists a periodic double-

layer structure, as manifested by the continued presence of the Bragg peak at $Q_z = 1.33 \text{ nm}^{-1}$. A reduced number of layers or reduced homogeneity in layer thickness corresponds to the disappearance of Kiessig fringes between $Q_z = 0.99$ and 1.33 nm^{-1} . Further, the reduced density of the uppermost Ta layer in Fig. 2 c) is corroborated by the reduction of the $Q_z = 0.87 \text{ nm}^{-1}$ peak that is replaced by the $Q_z \sim 0.81 \text{ nm}^{-1}$ peak. Finally, front expanding plasmas are inferred by a new shoulder appearing at $Q_z = 0.73 \text{ nm}^{-1}$.

This method allows us to quantitatively investigate the density dynamics in the surface region as summarized in Figs. 3 a-c). From that, we can extract several important physical parameters to describe the energy transport. For example, the velocity of the density perturbation front propagating into bulk, indicated by the vertical dashed

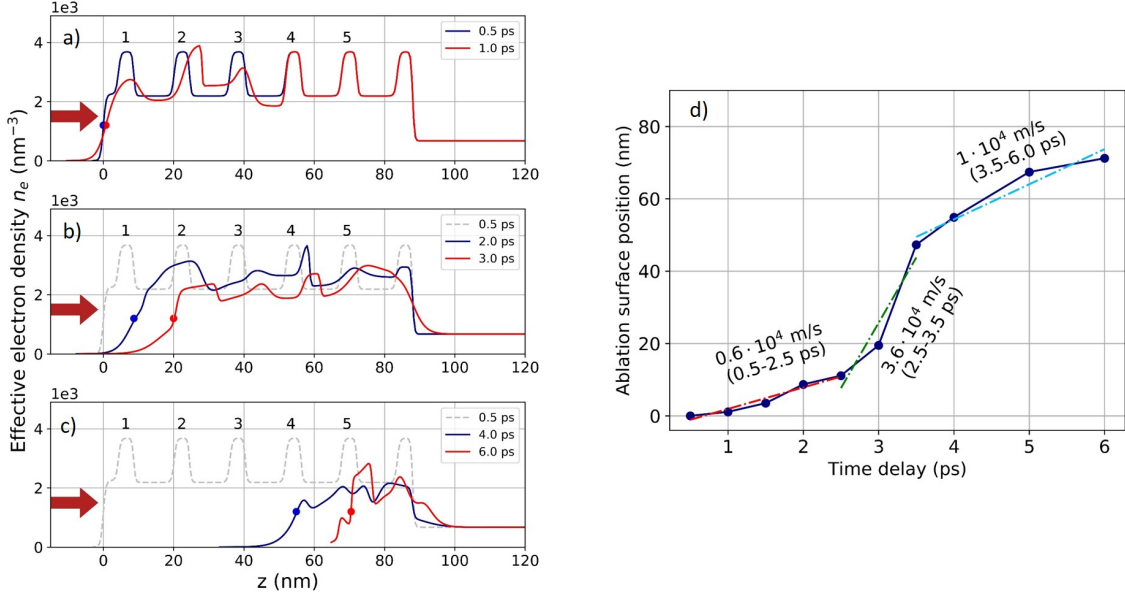


FIG. 3. **Evolution of the electron density depth profiles extracted from the GISAXS data and ablated surface positions.** a-c) The effective electron density profile vs. depth after the laser irradiation with delays of a) 0.5 ps and 1.0 ps, b) 2.0 and 3.0 ps and c) 4.0 and 6.0 ps, respectively. The laser comes from the left. The x-ray and laser parameters are same as Fig. 1 and 2. The grey dashed lines in b) and c) represent the initial density profile. The vertical dashed line in a) and b) represent positions of the density perturbation front at each delay, which indicate the propagation speed of $5 \times 10^4 \text{ m/s}$. The ablation surface is defined as the position where the density drops half of the initial Cu_3N density, as indicated by circles in a-c). d) Ablation surface position vs. time and corresponding velocities.

line in Fig. 3 a-b), yields $\sim 5 \times 10^4 \text{ m/s}$ which shows a good agreement with the velocity of the electronic heat diffusion as described below. The hydrodynamic simulation (*Methods*) predicts a surface electron temperature after the laser pulse of $T_e \sim 20 \text{ eV}$ (Fig. 4 a, and *Methods*) which decreases to below 10 eV after 1 ps. Those temperatures are close to the Fermi temperature ($T_F = 15$ and 11 eV for Ta^{5+} and Cu^{2+} , respectively) where the collision frequency has its peak value ($\nu_{ei} \sim \omega_{pe} \geq 10^{16} \text{ s}^{-1}$) [44, 45]. Here, ω_{pe} and ν_{ei} are the plasma frequency and the electron-ion collision frequency, respectively. This yields an electron mean free path of $< 1 \text{ nm}$ which suppresses ballistic electron transport into deep layers (see *Methods* for more details). In addition, because the temperature decays quickly after the laser pulse, the compression wave cannot take over the heat diffusion,

as confirmed by the experimentally observed density peaks at the second and fourth Ta layers at 1.0 and 2.0 ps delay, respectively, which propagate behind the density perturbation front (Fig. 3 a-b). The dominant energy transport is therefore driven by the heat diffusion that is expressed by the two-temperature (T_e, T_i for electrons and ions, respectively) energy conservation equations:

$$\begin{aligned} C_e \frac{\partial T_e}{\partial t} &= -\nabla \cdot \mathbf{q} - \gamma(T_e - T_i) + Q(z, t), \\ C_i \frac{\partial T_i}{\partial t} &= \gamma(T_e - T_i), \end{aligned} \quad (1)$$

where C_e, C_i are, respectively, the volumetric heat capacity of electrons and ions, $\mathbf{q} = \kappa \nabla T_e$ describes the electron thermal heat flow with $\kappa(\nu_{ei})$ being the heat conductivity, and $Q(z, t) = \partial I_{abs} / \partial z$ is the power density deposited by the laser with I_{abs}

being the absorbed laser flux. The energy transfer rate from electrons to ions is expressed by $\gamma = C_i \tau_i^{-1}$ with $\tau_i = m_i / (2m_e \nu_{ei})$ being the characteristic time for ion heating, where m_i , m_e are the electron and ion masses, respectively. With the hydrodynamic simulation, the position of the heat wave front was defined as $1/e$ of the surface temperature at each time frame shown in Fig. 4 a). From that, we obtain the heat wave speed of $\sim 6 \times 10^4$ m/s as plotted in Fig. 4 c), which shows a good agreement with the speed of the density perturbation front observed in the experiment (Fig. 3 a-b)).

The observed subsurface density evolution also yields the ablation dynamics. Here, the ablation surface is defined as the position where the density drops to half of the initial Cu density, as indicated by circles in Figs. 3 a-c). As summarized in Fig. 3 d), the ablation is initially slow and limited within the skin layer which then accelerates after 2.5 ps. We correlate these dynamics to the finite ion-heating time τ_i (5.5 ps and 2.5 ps for Ta⁵⁺ and Cu²⁺ for $\nu_{ei} = \omega_{pe}$, respectively). As reported previously, short-pulse laser ablation can be separated into multiple phases [46, 47]. First, photoelectric emission occurs immediately after the electrons acquire enough energy to overcome the work function E_W (4 – 5 eV for Ta and Cu [48]), the energy difference between the most energetic electrons in the conduction band and the continuum. These electrons drag ions by the electrostatic force, but this process is essentially limited within the skin layer. Second, more efficient mass ablation starts when the ions gain enough energy from the electrons to overcome their binding energy (4.2 and 3.5 eV for Ta and Cu, respectively). As shown in Fig. 4 b), the simulation indicates that this timescale is about 3 ps, in good agreement with our experimental observation. The ablation velocity observed in our experiment ($0.5 - 3.6 \times 10^4$ m/s, Fig. 3 d) also shows fair agreement with the sound velocity, *i.e.*, $C_s = 0.8 - 1.5 \times 10^4$ m/s at $T_e = 15$ eV (*see Methods for details*).

In contrast to that above, we observed that the measured density dynamics of each ML does not quantitatively agree with the hydrodynamic simulation; *i.e.*, the Ta layers persist much longer in the simulation compared with the experiment. We attribute this to the interpenetration of ion par-

ticles into adjacent layers, which starts once they gain enough kinetic energy from electrons via collisions. Such kinetic effects are inherently excluded in the hydrodynamic code that we used here, where the interfaces between Lagrangian cells needs to be preserved [45, 49]. In addition, the exact collision frequency, equation of state, heat capacity, and ionization model are not very well known near T_F . Those factors are intrinsically interconnected to each other in a non-trivial way to determine the temperature, pressure and thermodynamic phase which drive the density dynamics. To what extent each of these uncertainties affect the subsurface plasma dynamics is under investigation and will be reported in a more specialized publication – together with a kinetic code (*e.g.* particle-in-cell), which can treat particles individually.

To conclude, we measured the ultrafast subsurface density dynamics of solids upon intense laser irradiation with nanometer depth resolution and high sensitivity by detecting a diffusely scattered femtosecond x-ray beam at grazing incidence. By using a multi-layer sample, details of both the surface evolution and the energy transport into the bulk were obtained in a single x-ray pulse. Our new technique is sensitive enough to provide experimental data to benchmark various models and simulations of high-density, non-equilibrium plasmas with significantly higher precision than previously possible. The technique could also provide new insights into laser ablation for applications in nano-fabrication, removal of dental enamel or art restoration [46], as well as have a large impact on warm-dense-matter research [20] and (relativistic) plasma optics [14]. Furthermore, the grazing-incidence x-ray technique also contains information on the surface and interface roughnesses, and the density correlations (*see Supplementary Information*) [36]. This allows in-depth study of the development of surface roughness, ripples [50], laser-induced periodic surface nanostructures (LIPSS) [51], surface plasma instability [52], as well as characterization of the spatial homogeneity of shock waves propagating into solids [32, 33]. The accessible Q -range can be enhanced simply by utilizing a larger detection area which would provide further constraints on the density retrieval. We have verified that the signal is intense enough up to at least $Q = 2.5 \text{ nm}^{-1}$. Finally, the tempo-

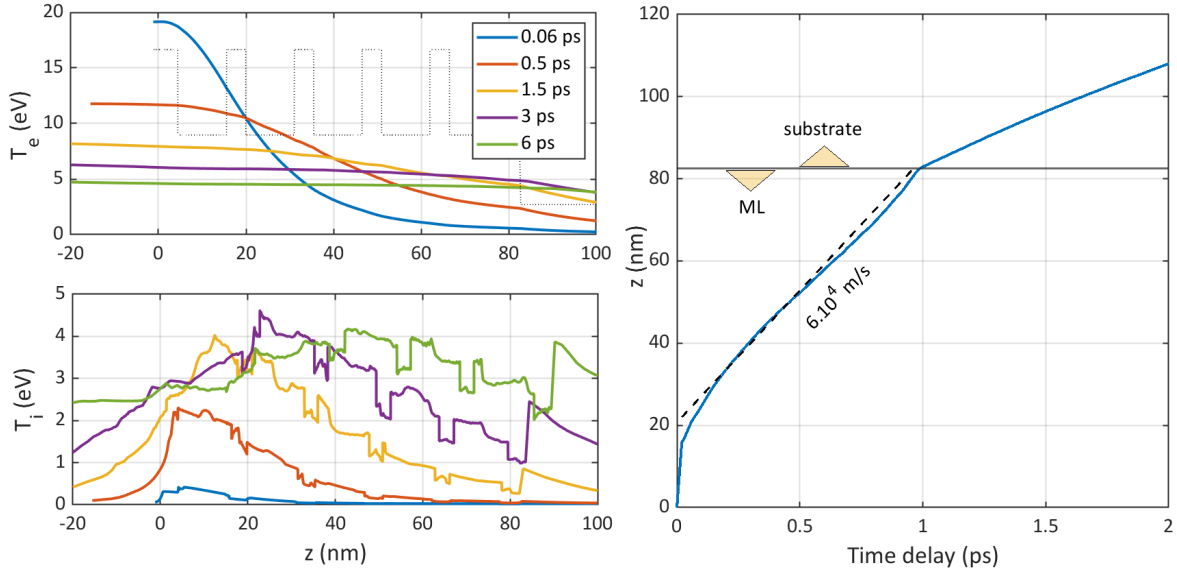


FIG. 4. **Electron and ion temperature evolution calculated by the hydrodynamic simulation.** Calculated with the Multi-fs hydrodynamic simulation (see *Methods*). The laser is irradiated from the left side and a depth of $z = 0$ corresponds to the initial solid surface. The laser intensity is 3.6×10^{14} W/cm² with 50 fs duration FWHM, 17° angle of incidence from the target normal, p-polarization. Laser intensity peak is at 60 fs. **a)** Electron temperature T_e vs. depth. The black dotted line indicates the initial solid density (arbitrary units). **b)** Ion temperature T_i vs. depth. The colour code of each line is same as a). **c)** Position of the heat front, defined as the $1/e$ of the peak temperature obtained by a) at each time frame. It arrives at the end of the ML at 1 ps, indicating an average velocity of $\sim 6 \times 10^4$ m/s.

ral resolution can be further improved ultimately down to the pulse duration of the few-femtosecond x-ray beam by employing a smaller x-ray beam size, or a collinear geometry between the pump laser and x-ray probe, for example with a final laser focusing mirror with a central hole.

METHODS

Experimental setup, x-ray and laser parameters

The experiment was performed at the SACLA XFEL facility in Japan at the Experimental Hutch 6 (EH6) which features a high-intensity optical laser ($\lambda_L = 800$ nm central wavelength, maximum 10 J/pulse with 40 fs duration in full-width half-maximum (FWHM)) combined with ultrashort intense x-ray pulses [34]. The x-ray pulses have a photon energy of 8.81 keV (with 43 eV FWHM

bandwidth), ~ 100 μ J/pulse, and a pulse duration of 7 fs in FWHM. The x-rays are focused to a 4 μ m FWHM spot on sample by a set of compound refractive lenses placed 3 m upstream from the sample. The scattered x-ray signal is recorded on a MPCCD area detector with 50 μ m pixel size [35] placed at a distance of 1.27 m from the sample and shielded by a 50 μ m thick Al foil, to remove any plasma-induced Bremsstrahlung background. The incident angle is fixed at 0.64° to be slightly larger than the critical angle of total external reflection $\alpha_c \propto \sqrt{n_e}$ for both Ta ($\alpha_{c,Ta} = 0.46^\circ$) and Cu ($\alpha_{c,Cu} = 0.35^\circ$). The photon energy was chosen not to overlap with any x-ray absorption edges or resonant lines of both Cu and Ta. The closest edges were 8.98 keV for the Cu K-edge and 9.88 keV for the Ta L-III edge. When the ionization develops with temperature, bound-bound absorption may appear: namely the 1s-3p transition in Cu around 8.95 keV at $T_e \geq 75$ eV and 2s-4f

transition in Ta around 9.7 keV at $T_e \geq 90$ eV [42]. Nevertheless, these transitions are still far enough from our x-ray photon energy. Therefore, we neglected the dispersion correction terms for our x-ray analysis. The x-ray probe is sensitive to the electrons with binding energies below the photon energy, i.e., 27 and 63 electrons for Cu(29) and Ta(73), respectively (total electrons in parenthesis). The sample is irradiated by a high-intensity optical laser attenuated to deliver ~ 53 mJ energy/pulse, impinging on the sample at 17° incident angle from the surface normal with p-polarization. In order to cover the x-ray footprint on sample ($4\ \mu\text{m}$ FWHM for 0.64° grazing incidence yields $360\ \mu\text{m}$), the optical laser beam is defocused to a diameter of $\sim 500\ \mu\text{m}$ yielding an average laser intensity of about 3.6×10^{14} W/cm² (see *Supplementary Information*).

Multilayer sample and its characterization

The multilayer (ML) sample was prepared by DC magnetron sputtering at the University of Mainz. Five repeated layers of Ta and Cu₃N were grown onto a thick silicon wafer carrying a Ta seed layer on a 100 nm thick layer of thermal silicon oxide, yielding a ML structure of, from the laser irradiation side, 5 repeat of Ta(4.3 nm thick)/Cu₃N(11.5 nm), Ta(4.3 nm), SiO₂(100 nm) and Si substrate(700 μm). The wafer was then laser-cut into 4×7 mm² individual pieces. Each sample was mounted on a rotation wheel which was individually pre-aligned with an attenuated x-ray FEL beam. Then we fixed the grazing incident angle to $\alpha_i = 0.64^\circ$ corresponding to the intense first ML Bragg peak at $Q_z = 0.99\ \text{nm}^{-1}$. This geometry, together with the size of the vacuum window and of the detector, allowed us to cover a Q -range of up to $1.5\ \text{nm}^{-1}$. The strong specular signal at the exit angle $\alpha_f = 0.64^\circ$ is blocked by a 3 mm diameter tungsten beam stop. The high visibility of the GISAXS signal indicates that our ML sample has a high degree of vertical correlation between the interfaces. The samples were pre-characterized at Technische Universität Dortmund with an x-ray reflectometry using a $\theta - 2\theta$ reflectometer [53]. For the measurement, the sample was mounted on an angle-dispersive reflectometer for angle adjustment between the sample and detector circle. This al-

lows us to characterize the exact layer thickness (from the angular difference between the Kiessig oscillations), number of repeated layers (from the number of Kiessig fringes), surface roughness (from the overall reflectivity amplitude), and the average density of a layered system (from the critical angle of total external reflection, α_c). Additional description as well as measured reflectivity curve is in the *Supplementary Information*, Fig. S4. The retrieved surface and interface roughness was 3–6 Å (root-mean-square value) depending on each layer.

Hydrodynamic simulation

We used a hydrodynamic simulation Multi-fs [45, 49] specifically designed for short (\leq ps) pulse high-intensity laser-solid interactions below $< 10^{17}$ W/cm² laser intensity. The code calculates an explicit solution for Maxwell's equation for the interaction of the laser pulse with the steep density gradient in the plasma, and includes the temperature-dependent collision frequency as well as the thermal conductivity from metallic solid up to the high-temperature plasma, with separate equations for electron and ions (two-temperature model). In order to generate an equation-of-state (EOS) table, we used the FEOS code [54] based on a QEOS description [55]. The ionization state is obtained by the SNOF atomic code [56] for Ta, and by FEOS for Cu within the Thomas-Fermi description. 1020 cells were used for simulating the target which includes 820 cells for the multilayers (82 nm thick) and 200 cells for the $5\ \mu\text{m}$ thick substrate, respectively. Furthermore, to reduce the numerical error, we used finer cells closer to the surface and interfaces and wider cells in the middle of each multilayer. For the substrate material, we use aluminium (Al) instead of silicon. The faster increase of the ion temperature in the substrate shown in Fig. 4 b is due to the faster electron-to-ion energy exchange rate in Al compare to Ta and Cu.

Initial electron temperature at the surface

The laser energy is deposited primarily to free electrons in metal via inverse Bremsstrahlung (intra-band absorption) because of the high collision frequency. The average energy per electron in the

initial plasma can be estimated as follows. Assuming the laser absorption rate $\eta = 0.2$ for our laser intensity and quasi-normal incidence (which leads absorbed fluence of 2.9 J/cm^2) [44], the average electron temperature within the skin layer at the end of the laser pulse can be expressed as $T_e = \eta I_L \tau_L / (\delta_s C_e)$ where $\delta_s = 10.1 \text{ nm}$ is the collisionless skin depth of Ta^{5+} and $C_e = 1.5 k_B n_e$ with $n_e(\text{Ta}^{5+}) = 2.78 \times 10^{23} \text{ cm}^{-3}$ is the electron volumetric heat capacity for the ideal gas. This leads to $k_B T_e \sim 43 \text{ eV}$, which should be considered as the maximum threshold as the thermal conduction and ionization are neglected in this estimation. Our hydro-simulation predicts an initial temperature after the laser pulse (40 fs after the laser intensity peak) of 20 eV as shown in Fig. 4 a).

Collision frequency, velocities, electron mean free path

The energy of electrons in an oscillating electric field, or the ponderomotive potential is $e^2 E_L^2 / (4m_e \omega_L^2) = 9.3 \times 10^{-14} I_L \lambda_L^2$, with I_L and λ_L in W/cm^2 and μm , respectively. At $3.6 \times 10^{14} \text{ W/cm}^2$, this energy is 21 eV. The collision frequency ν_{ei} between electrons and ions (or phonons) is one of the most important physical quantity to describe the energy transport. The precise value of ν_{ei} around the Fermi temperature (T_F) is as of yet unknown, and interpolated formulae between metal-like solids ($\nu_{e\text{-phonons}} \propto T_e$) and ideal gas plasmas ($\nu_{ei} \propto T_e^{-1.5}$) are often used [45]. Around T_F , the collision frequency reaches its maximum value, close to the plasma frequency $\omega_{pe} = 5.64 \sqrt{n_{free}} = 3.0 \times 10^{16}, 2.3 \times 10^{16} \text{ rad/s}$, for cold Ta^{5+} and Cu^{2+} , respectively. The velocity of individual electrons around or below T_F in a metal is $v_F = \hbar(3\pi^2 n_{free})^{1/3} / m_e$, which is 2.3×10^6 and $2.0 \times 10^6 \text{ m/s}$ for Ta^{5+} and Cu^{2+} , respectively (\hbar is the Planck's constant). At $T_e > T_F$, the thermal electron velocity $v_{th} = \sqrt{k_B T_e / m_e}$ needs to be considered, which leads to an electron velocity of $v_e = \sqrt{v_F^2 + 3v_{th}^2}$. At $T_e = 20 \text{ eV}$, it leads $v_e = 4.0 \times 10^6$ and $3.8 \times 10^6 \text{ m/s}$, for Ta^{5+} and Cu^{2+} , respectively. A corresponding electron mean free path is $v_e / \nu_{ei} \sim 0.1 - 0.2 \text{ nm}$, which is significantly smaller than the skin depth. Under these conditions, ballistic transport of electrons is effectively suppressed and the diffusion approxima-

tion for the electron heat transfer can be assumed.

Sound velocity

The sound velocity is the speed of an ion-density modulation driven by the pressure wave. Assuming the ideal gas equation of state (EOS), the sound velocity can be expressed as,

$$C_s = \sqrt{\frac{\gamma_e Z_{mean} k_B T_e + \gamma_i k_B T_i}{M_i}},$$

where Z_{mean} is the mean ionization, γ_e and γ_i are adiabatic index of electrons and ions, respectively and $M_i = 181 \text{ a.u.}$ and 63 a.u. is the ion mass for Ta and Cu, respectively. From the ideal gas EOS, $\gamma = 1 + 2/n$ with n being the number of degrees of freedom. In most cases, $\gamma_e = 1$ and $\gamma_i = 3$ can be used. As an example, for $(T_e, T_i) = (20, 5) \text{ eV}$ and $Z_{mean} = 5$, $C_{s_Ta} = 7.8 \times 10^3 \text{ m/s}$ and $C_{s_Cu} = 1.5 \times 10^4 \text{ m/s}$, respectively.

Acknowledgements

The XFEL experiments were performed at the BL2 of SACLA with the approval of the Japan Synchrotron Radiation Research Institute (JASRI) (Proposal No. 2018B8049). C.G. acknowledges funding by DFG GU 535/6-1. G.J., M.V.-K and M.K acknowledge support by the EU (FETS-Nebula #863155) and the ERC (SyG 3D MAGiC #856538). A.K acknowledges support by JST-Mirai Program Grant Number JPMJMI17A1, Japan. C.R. is supported by the LOEWE excellence initiative of the state of Hesse. We acknowledge invaluable input from C. Bantzt (HZDR) for sample alignment and data interpretation. M.Na. thanks R. Kodama (U. Osaka), Th. Tschentscher, U. Zastrau (EuXFEL) and M. Yabashi (RIKEN) for their useful advices. M.Ba and M.Na thank E. Brambrink (EuXFEL) for valuable advice for hydrodynamic simulation. We thank A. Pelka, L. G. Huang (HZDR), and J-P. Schwinkendorf (EuXFEL) for various discussions. We acknowledge the support of M. Spiwek (DESY) and DISCO HI-TEC EUROPE GmbH for cutting ML samples.

Author Contributions

C.G. and M.Na. conceived the study. L.R., M.Ba., T.R.P., M.M., N.P.D., S.G., T.M., M.Ni., C.G., and M.Na performed the experiment at SACLA with support from T.Y., Y.I., K.S., and T.T. L.R. analyzed the GISAXS data under the supervision of C.G. M.Ba performed hydrodynamic simulation to interpret the data under the supervision and support of Y.S., C.F-G, T.K, A.P.M, M.Bu, T.E.C and M.Na., with additional support from N.P.D. and J.K.K. to generate EOS tables. Multilayer samples were prepared by G.J., M.V-K., and M.K. which were further characterized by L.R., F.S., D.K., and M.P. before the experiment. J.K., M.M. and M.Na organized the sample cutting. L.R, M.Ba, C.G, and M.Na wrote the paper with extensive suggestions from T.R.P., N.P.D., C.R. and T.K., which was further improved by input from T.Y., M.M., G.J., J.K.K., M.Ni., M.K., C.F-G, and A.P.M. All authors commented on the manuscript.

Data Availability

The datasets generated during and/or analysed during the current study are available from the corresponding author on reasonable request. Most of data generated or analysed during this study are included in its supplementary information files.

Code Availability

The codes used during the current study are available from the corresponding author on reasonable request.

Additional information

Supplementary Information is available in the online version of the paper. Reprints and permissions information is available online at xxx. Correspondence and requests for materials should be addressed to C.G. and M.Na.

* christian.gutt@uni-siegen.de

† motoaki.nakatsutsumi@xfel.eu

- [1] R. R. Gattass and E. Mazur, "Femtosecond laser micromachining in transparent materials," *Nature Photonics* **2**, 219–225 (2008).
- [2] K. C. Phillips, H. H. Gandhi, E. Mazur, and S. K. Sundaram, "Ultrafast laser processing of materials: a review," *Adv. Opt. Photon.* **7**, 684–712 (2015).
- [3] A. Rousse, C. Rischel, S. Fourmaux, I. Uschmann, S. Sebban, G. Grillon, Ph. Balcou, E. Förster, J. P. Geindre, P. Audebert, J. C. Gauthier, and D. Hulin, "Non-thermal melting in semiconductors measured at femtosecond resolution," *Nature* **410**, 65–68 (2001).
- [4] L. B. Fletcher, H. J. Lee, T. Döppner, E. Galtier, B. Nagler, P. Heimann, C. Fortmann, S. LePape, T. Ma, M. Millot, A. Pak, D. Turnbull, D. A. Chapman, D. O. Gericke, J. Vorberger, T. White, G. Gregori, M. Wei, B. Barbrel, R. W. Falcone, C.-C. Kao, H. Nuhn, J. Welch, U. Zastra, P. Neumayer, J. B. Hastings, and S. H. Glenzer, "Ultra-bright X-ray laser scattering for dynamic warm dense matter physics," *Nature Photonics* **9**, 274–279 (2015).
- [5] B. N. Chichkov, C. Momma, S. Nolte, F. Alvensleben, and A. Tünnermann, "Femtosecond, picosecond and nanosecond laser ablation of solids," *Applied Physics A Materials Science & Processing* **63**, 109–115 (1996).
- [6] B. Rethfeld, K. Sokolowski-Tinten, D. von der Linde, and S.I. Anisimov, "Timescales in the response of materials to femtosecond laser excitation," *Applied Physics A* **79**, 767–769 (2004).
- [7] P. Balling and J. Schou, "Femtosecond-laser ablation dynamics of dielectrics: basics and applications for thin films," *Reports on Progress in Physics* **76**, 036502 (2013).
- [8] D. Strickland and G. Mourou, "Compression of amplified chirped optical pulses," *Optics Communications* **56**, 219–221 (1985).
- [9] T. Brabec and F. Krausz, "Intense few-cycle laser fields: Frontiers of nonlinear optics," *Reviews of Modern Physics* **72**, 545–591 (2000).
- [10] S. Nolte, C. Momma, H. Jacobs, A. Tünnermann, B. N. Chichkov, B. Wellegehausen, and H. Welling, "Ablation of metals by ultrashort laser pulses," *Journal of the Optical Society of America B* **14**, 2716 (1997).
- [11] A. Y. Vorobyev and C. Guo, "Direct femtosecond laser surface nano/microstructuring and its applications," *Laser & Photonics Reviews* **7**, 385–407 (2013).

- [12] G. Doumy, F. Quéré, O. Gobert, M. Perdrix, Ph. Martin, P. Audebert, J. C. Gauthier, J.-P. Geindre, and T. Wittmann, “Complete characterization of a plasma mirror for the production of high-contrast ultraintense laser pulses,” *Phys. Rev. E* **69**, 026402 (2004).
- [13] M. Nakatsutsumi, A. Kon, S. Buffechoux, P. Audebert, J. Fuchs, and R. Kodama, “Fast focusing of short-pulse lasers by innovative plasma optics toward extreme intensity,” *Opt. Lett.* **35**, 2314–2316 (2010).
- [14] Henri Vincenti, “Achieving Extreme Light Intensities using Optically Curved Relativistic Plasma Mirrors,” *Phys. Rev. Lett.* **123**, 105001 (2019).
- [15] J. A. Wheeler, A. Borot, S. Monchocé, H. Vincenti, A. Ricci, A. Malvache, R. Lopez-Martens, and F. Quéré, “Attosecond lighthouses from plasma mirrors,” *Nature Photonics* **6**, 829–833 (2012).
- [16] H. Daido, M. Nishiuchi, and A. S. Pirozhkov, “Review of laser-driven ion sources and their applications,” *Rep. Prog. Phys.* **75**, 056401 (2012); Andrea Macchi, Marco Borghesi, and Matteo Passoni, “Ion acceleration by superintense laser-plasma interaction,” *Rev. Mod. Phys.* **85**, 751–793 (2013).
- [17] D. J. Stark, T. Toncian, and A. V. Arefiev, “Enhanced Multi-MeV Photon Emission by a Laser-Driven Electron Beam in a Self-Generated Magnetic Field,” *Phys. Rev. Lett.* **116**, 185003 (2016).
- [18] S. C. Wilks, W. L. Kruer, M. Tabak, and A. B. Langdon, “Absorption of ultra-intense laser pulses,” *Phys. Rev. Lett.* **69**, 1383–1386 (1992).
- [19] L. Chopineau, A. Leblanc, G. Blaclair, A. Denoed, M. Thévenet, J.-L. Vay, G. Bonnaud, Ph. Martin, H. Vincenti, and F. Quéré, “Identification of Coupling Mechanisms between Ultraintense Laser Light and Dense Plasmas,” *Phys. Rev. X* **9**, 011050 (2019).
- [20] B. A. Remington, R. P. Drake, H. Takabe, and D. Arnett, “A review of astrophysics experiments on intense lasers,” *Physics of Plasmas* **7**, 1641–1652 (2000).
- [21] S. Atzeni and J. Meyer-ter Vehn, *The physics of inertial fusion: Beam plasma interaction, hydrodynamics, hot dense matter* (Oxford: Clarendon Press, 2004).
- [22] K. Sokolowski-Tinten, J. Bialkowski, A. Cavalleri, D. von der Linde, A. Oparin, J. Meyer-ter Vehn, and S. I. Anisimov, “Transient States of Matter during Short Pulse Laser Ablation,” *Physical Review Letters* **81**, 224–227 (1998).
- [23] J. P. Geindre, P. Audebert, A. Rousse, F. Fallières, J. C. Gauthier, A. Mysyrowicz, A. Dos Santos, G. Hamoniaux, and A. Antonetti, “Frequency-domain interferometer for measuring the phase and amplitude of a femtosecond pulse probing a laser-produced plasma,” *Opt. Lett.* **19**, 1997–1999 (1994).
- [24] M. Bocoum, F. Böhle, A. Vernier, A. Jullien, J. Faure, and R. Lopez-Martens, “Spatial-domain interferometer for measuring plasma mirror expansion,” *Optics Letters* **40**, 3009 (2015).
- [25] A. Malvache, A. Borot, F. Quéré, and R. Lopez-Martens, “Coherent wake emission spectroscopy as a probe of steep plasma density profiles,” *Phys. Rev. E* **87**, 035101 (2013).
- [26] C. W. Siders, “Detection of Nonthermal Melting by Ultrafast X-ray Diffraction,” *Science* **286**, 1340–1342 (1999).
- [27] K. Sokolowski-Tinten, C. Blome, J. Blums, A. Cavalleri, C. Dietrich, A. Tarasevitch, I. Uschmann, E. Förster, M. Kammler, M. Horn-von Hoegen, and D. von der Linde, “Femtosecond X-ray measurement of coherent lattice vibrations near the Lindemann stability limit,” *Nature* **422**, 287–289 (2003).
- [28] A. Cavalleri, Cs Tóth, C. W. Siders, J. A. Squier, F. Ráksi, P. Forget, and J. C. Kieffer, “Femtosecond Structural Dynamics in VO₂ during an Ultrafast Solid-Solid Phase Transition,” *Physical Review Letters* **87**, 237401 (2001).
- [29] R. I. Tobey, M. E. Siemens, O. Cohen, M. M. Murnane, H. C. Kapteyn, and K. A. Nelson, “Ultrafast extreme ultraviolet holography: dynamic monitoring of surface deformation,” *Opt. Lett.* **32**, 286–288 (2007).
- [30] T. Gorkhover, S. Schorb, R. Coffee, M. Adolph, L. Foucar, D. Rupp, A. Aquila, J. D. Bozek, S. W. Epp, B. Erk, L. Gumprecht, L. Holmegaard, A. Hartmann, R. Hartmann, G. Hauser, P. Holl, Andre H., N. Kimmel, K.-U. Kühnel, M. Messerschmidt, Ch. Reich, A. Rouzée, B. Rudek, C. Schmidt, J. Schulz, H. Soltau, S. Stern, G. Weidenspointner, B. White, J. Küpper, L. Strüder, I. Schlichting, J. Ullrich, D. Rolles, A. Rudenko, T. Möller, and Ch. Bostedt, “Femtosecond and nanometre visualization of structural dynamics in superheated nanoparticles,” *Nature* **10**, 93–97 (2016).
- [31] T. Kluge, M. Rödel, J. Metzkes-Ng, A. Pelka, A. L. Garcia, I. Prencipe, M. Rehwald, M. Nakatsutsumi, E. E. McBride, T. Schönherr, M. Garten, N. J. Hartley, M. Zacharias, J. Grenzer, A. Erbe, Y. M. Georgiev, E. Galtier, I. Nam, H. J. Lee, S. Glenzer, M. Bussmann, C. Gutt, K. Zeil, C. Rödel, U. Hübner, U. Schramm, and T. E. Cowan, “Observation of Ultrafast Solid-Density Plasma Dynamics Using Femtosecond X-Ray Pulses from a Free-Electron Laser,” *Phys. Rev. X* **8**, 031068 (2018).
- [32] A. Schropp, R. Hoppe, V. Meier, J. Patommel, F. Seiboth, Y. Ping, D. G. Hicks, M. A. Beckwith,

- G. W. Collins, A. Higginbotham, J. S. Wark, H. J. Lee, B. Nagler, E. C. Galtier, B. Arnold, U. Zastrau, J. B. Hastings, and C. G. Schroer, “Imaging Shock Waves in Diamond with Both High Temporal and Spatial Resolution at an XFEL,” *Scientific Reports* **5**, 11089 (2015).
- [33] F. Barbato, S. Atzeni, D. Batani, D. Bleiner, G. Boutoux, C. Brabetz, P. Bradford, D. Manelli, P. Neumayer, A. Schiavi, J. Trela, L. Volpe, G. Zeraouli, N. Woolsey, and L. Antonelli, “Quantitative phase contrast imaging of a shock-wave with a laser-plasma based X-ray source,” *Scientific Reports* **9**, 1 (2019).
- [34] T. Yabuuchi, A. Kon, Y. Inubushi, T. Togahi, K. Sueda, T. Itoga, K. Nakajima, H. Habara, R. Kodama, H. Tomizawa, and M. Yabashi, “An experimental platform using high-power, high-intensity optical lasers with the hard X-ray free-electron laser at SACLA,” *J. Sync. Rad.* **26**, 585–594 (2019).
- [35] T. Kameshima, S. Ono, T. Kudo, K. Ozaki, Y. Kirihara, K. Kobayashi, Y. Inubushi, M. Yabashi, T. Horigome, A. Holland, K. Holland, D. Burt, H. Murao, and T. Hatsui, “Development of an X-ray pixel detector with multi-port charge-coupled device for X-ray free-electron laser experiments,” *Review of Scientific Instruments* **85**, 033110 (2014).
- [36] V. Holý, J. Kuběna, I. Ohlídal, K. Lischka, and W. Plotz, “X-ray reflection from rough layered systems,” *Phys. Rev. B* **47**, 15896–15903 (1993).
- [37] H. Kiessig, “Untersuchung zur Totalreflexion von Röntgenstrahlen,” *Annalen der Physik* **10**, 769 (1931).
- [38] Y. Yoneda, “Anomalous Surface Reflection of X Rays,” *Phys. Rev.* **131**, 2010–2013 (1963).
- [39] S. K. Sinha, E. B. Sirota, S. Garoff, and H. B. Stanley, “X-ray and neutron scattering from rough surfaces,” *Phys. Rev. B* **38**, 2297–2311 (1988).
- [40] U. Pietsch, V. Holý, and T. Baumbach, *High-resolution x-ray scattering* (Springer, New York, NY, 2004).
- [41] A. Hexemer and P. Müller-Buschbaum, “Advanced grazing-incidence techniques for modern soft-matter materials analysis,” *IUCrJ* **2**, 106–125 (2015).
- [42] H.-K. Chung, M.H. Chen, W.L. Morgan, Y. Ralchenko, and R.W. Lee, “FLYCHK: Generalized population kinetics and spectral model for rapid spectroscopic analysis for all elements,” *High Energy Density Physics* **1**, 3 – 12 (2005).
- [43] G. Pospelov, W. Van Herck, J. Burle, J. M. Carmona Loaiza, C. Durniak, J. M. Fisher, M. Ganeva, D. Yurov, and J. Wuttke, “*BornAgain*: software for simulating and fitting grazing-incidence small-angle scattering,” *Journal of Applied Crystallography* **53**, 262–276 (2020).
- [44] D. Fisher, M. Fraenkel, Z. Henis, E. Moshe, and S. Eliezer, “Interband and intraband (Drude) contributions to femtosecond laser absorption in aluminum,” *Phys. Rev. E* **65**, 016409 (2001).
- [45] K. Eidmann, J. Meyer-ter Vehn, T. Schlegel, and S. Hüller, “Hydrodynamic simulation of subpicosecond laser interaction with solid-density matter,” *Phys. Rev. E* **62**, 1202–1214 (2000).
- [46] E.G. Gamaly, “The physics of ultra-short laser interaction with solids at non-relativistic intensities,” *Phys. Rep.* **508**, 91–243 (2011).
- [47] J. Reif, “Basic physics of femtosecond laser ablation,” in *Laser-Surface Interactions for New Materials Production: Tailoring Structure and Properties*, edited by Antonio Miotello and Paolo M. Ossi (Springer Berlin Heidelberg, Berlin, Heidelberg, 2010) pp. 19–41.
- [48] H. B. Michaelson, “The work function of the elements and its periodicity,” *Journal of Applied Physics* **48**, 4729–4733 (1977).
- [49] R. Ramis, K. Eidmann, J. Meyer-ter Vehn, and S. Hüller, “MULTI-fs – A computer code for laser–plasma interaction in the femtosecond regime,” *Comp. Phys. Comm.* **183**, 637–655 (2012).
- [50] A. Sgattoni, S. Sinigardi, L. Fedeli, F. Pegoraro, and A. Macchi, “Laser-driven Rayleigh-Taylor instability: Plasmonic effects and three-dimensional structures,” *Phys. Rev. E* **91**, 013106 (2015).
- [51] J. Bonse and S. Gräf, “Maxwell Meets Marangoni – A Review of Theories on Laser-Induced Periodic Surface Structures,” *Laser and Photonics Reviews* **14**, 2000215 (2020).
- [52] T. Kluge, J. Metzkes, K. Zeil, M. Bussmann, U. Schramm, and T. E. Cowan, “Two surface plasmon decay of plasma oscillations,” *Physics of Plasmas* **22**, 064502 (2015).
- [53] C. Krywka, C. Sternemann, M. Paulus, M. Volmer, U. Berges, and M. Tolan, “Experimental Endstation of Beamline BL9 at DELTA,” *AIP Conference Proceedings* **879**, 875–878 (2007).
- [54] S. Faik, A. Tauschwitz, and I. Iosilevskiy, “The equation of state package FEOS for high energy density matter,” *Comput. Phys. Comm.* **227**, 117 – 125 (2018).
- [55] R. M. More, K. H. Warren, D. A. Young, and G. B. Zimmerman, “A new quotidian equation of state (qeos) for hot dense matter,” *The Physics of Fluids* **31**, 3059–3078 (1988).
- [56] K. Eidmann, “Radiation transport and atomic physics modeling in high-energy-density laser-produced plasmas,” *Las. Part. Beams* **12**, 223–244 (1994).